Numerical Simulation of the Aerodynamics and Acoustics of a Turbulent Wall Jet with Particulates

Wei Wang,* Trushant Patel,† S. Balachandar,‡ and S. A. E. Miller§
University of Florida

Understanding sound generation from high-speed multiphase jet flow is important for designing rocket engines and launch pad structures. We present a numerical approach for predicting far-field noise from a multiphase supersonic jet flow. We numerically evaluate the Navier-Stokes equations with two-way coupling of Lagrangian particle tracking. The far-field acoustic pressure is evaluated using the Ffowcs-Williams and Hawkings acoustic analogy. We conduct predictions for flows emerging from a converging-diverging rectangular nozzle operating at over-expanded, under-expanded, and on-design conditions. The nozzle exit is connected to a large flat plate. Both single phase and multiphase predictions are conducted, and the multiphase flow consists of a gas phase and particulates. Multiphase calculations are performed using particles with diameters of 10 μm and 100 μm. We validate the predictions of the single phase jet flows with measurement. We compare meanflows, turbulent statistics, acoustic source statistics, and statistics of acoustic pressure between the single and multiphase jets. We find that there are significant differences of predicted statistics between single and multiphase jets.

Nomenclature

Symbols

c	local speed of sound
$c_{p,p}$	specific heat of the particle
c_∞	ambient speed of sound
D_e	equivalent nozzle exit diameter
d_p	diameter of the particle
E	total energy
E_p	energy source from particles
$\boldsymbol{F}_c$	convective flux vector
$\boldsymbol{F}_v$	viscous flux vector
$f_{e,i}$	external volumetric forces
$f_{p,i}$	momentum source from particles
$g(x,t)$	function representing FWH surface
H	total enthalpy
$\mathcal{H}(x)$	Heaviside function
h_e	nozzle exit height
h_i	nozzle inlet height
h_t	nozzle throat height
k	thermal conductivity
ℓ_i	local force on the FWH surface
m_p	mass source of particles
$\boldsymbol{n}$	face normal vector
$\boldsymbol{n'}$	face normal vector from FWH surface
p	pressure
p'	pressure fluctuations
p_∞	ambient static pressure
$\boldsymbol{Q}$	source term vector
$\dot{q}_h$	external heat source
R	gas constant
$\boldsymbol{r}$	vector from FWH surface to observer position
S_{ij}	strain rate tensor
T	temperature
T_∞	ambient static temperature
T_p	temperature of particle
$\mathcal{T}_{ij}$	Lighthill's stress tensor
t	time
$\boldsymbol{\mathcal{U}}$	FWH surface velocity vector
$\boldsymbol{V}$	velocity vector
V_n	face normal velocity
$\boldsymbol{V_p}$	velocity vector of the particle
$\boldsymbol{\mathcal{V}}$	FWH surface flow velocity vector
$\boldsymbol{W}$	conservative variable vector
w_e	nozzle spanwise width
$\boldsymbol{x_p}$	particle position vector

Greek Symbols

δ_{ij}	Kronecker delta
$\delta(x)$	Dirac delta function
θ	radiation angle from upstream nozzle axis
μ	dynamic viscosity
ν	kinematic viscosity
ρ	density
ρ_p	density of the particle
ρ'	density fluctuations
ρ_∞	ambient density
σ_{ij}	viscous stress tensor
τ	retarded time
τ_{ij}	shear stress tensor
τ^u	particle response time

*Ph.D. Candidate, Department of Mechanical and Aerospace Engineering, University of Florida, P.O. Box 116250, Gainesville, FL, 32611, USA, AIAA Student Member, wei.wang@ufl.edu

†Ph.D. Student, Department of Mechanical and Aerospace Engineering, University of Florida, P.O. Box 116250, Gainesville, FL, 32611, USA, AIAA Student Member, trushant@ufl.edu

‡Distinguished Professor, Department of Mechanical and Aerospace Engineering, University of Florida, P.O. Box 116250, Gainesville, FL, 32611, USA, AIAA Senior Member, bala1s@ufl.edu

§Assistant Professor, Department of Mechanical and Aerospace Engineering, University of Florida, P.O. Box 116250, Gainesville, FL, 32611, USA, AIAA Lifetime / Senior Member, saem@ufl.edu; saemiller@gmail.com

τ^θ	thermal response time
Ω	control volume
$d\Omega$	control surface

Non-Dimensional Numbers

M_d	design Mach number of nozzle
M_j	fully-expanded Mach number
M_∞	free-stream Mach number
$\boldsymbol{M}$	Mach number of FWH surface velocity vector
$\boldsymbol{\mathcal{M}}$	Mach number of flow velocity vector
Pr	Prandtl number
Re_p	particle Reynold's number
St	Strouhal number

Abbreviations

BBSAN	broadband shock-associated noise
CFD	computational fluid dynamics
FWH	Ffowcs-Williams Hawkings
LES	large eddy simulation
NPR	nozzle pressure ratio
PIV	particle image velocimetry
SPL	sound pressure level
TKE	turbulent kinetic energy
TTR	total temperature ratio

Introduction

High-speed heated off-design rocket exhaust contains particulates that result from the combustion process.[1–4] Noise from rocket and jet engine exhaust is extensively studied, and the source of sound is predominantly from turbulence and turbulent flow structures interacting with shock waves.[5–9] The particulates within the flow are convecting supersonically, interacting with the turbulence and shock waves, and are an additional source of acoustic radiation. Furthermore, the particulates alter the turbulence and have an effect on the shock cell structure.[10,11] These altered turbulent structures and variation of the shock cell structure, due to the particulates, change the radiated noise relative to an exhaust without particulates. The noise from rocket exhaust causes vibro-acoustic loading on the launch pad structure and the rocket itself. These acoustically induced vibrations result in sonic fatigue of the launch pad structure and flight vehicle.[12] In this paper, we present research to quantify the changes in acoustic radiation due to the addition of particulates within a high speed rocket exhaust.

Previous Experimental and Numerical Approaches

Fukuda et al.[13] performed a numerical study with a hybrid implicit large eddy simulation (LES) and Kirchoff method, and compared it with near-field and far-field acoustic data obtained from a stationary firing of a two stage solid rocket engine. They showed that the dominant component of noise is Mach wave radiation, generated by the fluctuations within the supersonic jet shear layer. Shur et al.[8] presented far-field noise predictions from single and dual-stream jets, operating at sonic and supersonic conditions, using two-stage implicit LES and Ffowcs-Williams and Hawkings (FWH) surface integral methods. Their prediction method was validated with measured data and showed good agreement. Heeb et al.[14] investigated supersonic jet flows from a low aspect ratio rectangular nozzle. They showed that screech tones were eliminated with elevated temperature for ideal, under-, and over-expanded conditions. The existence of crackle was shown to be highly correlated to far-field pressure skewness. Baier et al.[9] measured the velocity profile using Particle Image Velocimetry (PIV) of a convergent-divergent rectangular nozzle with a solid plate in the vicinity. As the solid plate approached the nozzle, the potential core grew larger and the maximum turbulent kinetic energy (TKE) decreased. Mora et al.[15] studied the effect of plate position on far-field noise from supersonic jets with rectangular nozzles. High amplitude noise at low frequency increased as the plate approached the jet plume. Broadband shock-associated noise (BBSAN) decreased as the plate approached the nozzle and was significantly weakened when the plate touched the nozzle lip line.

Present Approach

In this paper, we perform unsteady numerical simulations of a wall jet in conjunction with a FWH solver. The simulations are performed with the RocfluMP[16] computational fluid dynamics (CFD) code originally developed by the Center for Simulation of Advanced Rockets at the University of Illinois at Urbana-Champaign and extended at the Center for Compressible Multiphase Turbulence at the University of Florida. This code has been extensively used to simulate multiphase flow within rockets, jets, and plumes.[17–19] To simulate the effect of a large number of Lagrangian particles in the flow, we adopt "super particle," which represents a group of real particles with the same property. Acoustic predictions are performed with a FWH solver developed at the University of Florida using a modified form of Farassat's formulation 2B.[20] The unsteady aerodynamic simulations are compared and validated with the measurements of Baier et al.[9] Acoustic predictions are compared and validated with measurements of Mora et al.,[15] which have corresponding jet operating conditions of Baier et al.[9]

In the next section, we present our numerical method to predict the aerodynamics of the flow-field of a supersonic off-design wall jet. The FWH method and its implementation are then discussed. We perform two-dimensional simulation and far-field noise calculation for single phase and multiphase jet flow under different flow conditions with solid wall in close vicinity. Aerodynamic and aeroacoustic statistics of single phase wall jets are validated with experimental results. The impact of aluminum particles of diameter of 10 and 100 μm are studied under design condition corresponding to fully extended Mach number of 1.5. Comparisons of mean flow, turbulence and acoustic statistics of single phase and particle laden jet flow are shown in the the results section. Finally, we conclude our paper with a summary and conclusion.

Computational Approach

The prediction of the far-field noise from the jet exhaust is performed in two stages. In the first stage, an implicit LES simulation is conducted for ideal, under-, and over-expanded conditions. We adopt a two-way coupled Eulerian-Lagrangian approach to simulate the particle-laden flow at the ideally expanded conditions. The continuous phase, air, is treated with an Eulerian framework, while aluminum particles are tracked with Lagrangian representation. These particles alter the carrier phase by coupling with the momentum and energy equations. Field-variables are sampled every 10^{-5} seconds on an encompassing porous acoustic surface and subsequently used as input to the acoustic solver. The acoustic solver, which is described later, is based on the FWH equation and calculates the far-field fluctuating acoustic pressure. The sound pressure level (SPL) is derived using signal processing of the acoustic pressure. In the next section, we present the governing equations for the gas phase, particulates, and acoustics.

Gas Phase

We model the multiphase rocket exhaust using the filtered Navier-Stokes equations with additional source terms for particulates. The equations are written in integral-vector form as

$$\frac{\partial}{\partial t}\int_{\Omega} \boldsymbol{W} d\Omega + \oint_{\partial\Omega} \boldsymbol{F_c} dS = \oint_{\partial\Omega} \boldsymbol{F_v} dS + \int_{\Omega} \boldsymbol{Q} d\Omega, \tag{1}$$

where $\boldsymbol{F}_c$ is a vector of convective fluxes, $\boldsymbol{F}_v$ is a vector of viscous fluxes, $\boldsymbol{Q}$ is a vector source term, t is time, $\boldsymbol{W}$ is a vector of conservative variables, Ω represents volumetric integration, and $\partial\Omega$ represents a flux integral. The vectors $\boldsymbol{W}$, $\boldsymbol{F}_c$, and $\boldsymbol{F}_v$ are

$$\boldsymbol{W} = \Big[\rho, \rho u, \rho v, \rho w, \rho E\Big]^T, \tag{2}$$

$$\boldsymbol{F_c} = \Big[\rho V_n, \rho u V_n + n_x p, \rho v V_n + n_y p, \rho w V_n + n_z p, \rho H V_n\Big]^T, \tag{3}$$

and

$$\boldsymbol{F_v} = \begin{bmatrix} 0 \\ n_x\tau_{xx} + n_y\tau_{xy} + n_z\tau_{xz} \\ n_x\tau_{yx} + n_y\tau_{yy} + n_z\tau_{yz} \\ n_x\tau_{zx} + n_y\tau_{zy} + n_z\tau_{zz} \\ n_x\Theta_x + n_y\Theta_y + n_z\Theta_z \end{bmatrix}. \tag{4}$$

Here, E is total energy, H is total enthalpy, and the face normal velocity is $V_n = n_x u + n_y v + n_z w$, where $\boldsymbol{n} = [n_x, n_y, n_z]^T$ is the face normal vector. The shear stress tensor is defined as $\tau_{ij} = 2\mu S_{ij} - \frac{2}{3}\mu\frac{\partial v_k}{\partial x_k}\delta_{ij}$, where S_{ij} is the strain rate tensor, and μ is dynamic viscosity. Dynamic viscosity is computed from Sutherland's law, $\mu = \mu_{ref}(TT_{ref}^{-1})^{3/2}(T_{ref} + S)(T + S)^{-1}$, where $\mu_{ref} = 1.716 \times 10^{-5}$ kgm^{-1}s^{-1}, $T_{ref} = 273.15$ K, $S = 110.4$ K, and δ_{ij} is the Kronecker delta function. The vector $\boldsymbol{\Theta}$ is

$$\begin{aligned} \Theta_x &= u\tau_{xx} + v\tau_{xy} + w\tau_{xz} + k\frac{\partial T}{\partial x}, \\ \Theta_y &= u\tau_{yx} + v\tau_{yy} + w\tau_{yz} + k\frac{\partial T}{\partial y}, \\ \Theta_z &= u\tau_{zx} + v\tau_{zy} + w\tau_{zz} + k\frac{\partial T}{\partial z}, \end{aligned} \tag{5}$$

where k is the thermal conductivity and T is the temperature. This term represents the work of the viscosity and heat conduction. Finally, the vector $\boldsymbol{Q}$ is

$$\boldsymbol{Q} = \left[m_p, \rho f_{e,x} + f_{p,x}, \rho f_{e,y} + f_{p,y}, \rho f_{e,z} + f_{p,z}, \dot{q}_h + E_p\right]^T, \tag{6}$$

where E_p is the energy source from particles, $f_{e,i}$ are external volumetric forces, $f_{p,i}$ are momentum sources from particles, m_p is the mass source of particles, and $\dot{q}_h$ is the external heat source. The vector $\boldsymbol{Q}$ represents additional body forces and forces due to the particulates within the flow.

Pressure, temperature, and density are related through the ideal gas law

$$p = \rho R T, \tag{7}$$

where R is the gas constant.

Lagrangian Particles

The evolution equations for position, velocity, and temperature of a single Lagrangian particle are

$$\frac{d}{dt}\boldsymbol{x_p} = \boldsymbol{V_p}, \tag{8}$$

$$\frac{d}{dt}\boldsymbol{V_p} = \frac{\boldsymbol{V} - \boldsymbol{V}_p}{\tau^u}, \tag{9}$$

and

$$\frac{d}{dt}T_p = \frac{T - T_p}{\tau^\theta}, \tag{10}$$

where $\boldsymbol{x_p} = [x_p, y_p, z_p]^T$ is the position vector of the particle, $\boldsymbol{V} = [u_p, v_p, w_p]^T$ is the velocity vector of the gas at the particle position, $\boldsymbol{V_p}$ is the velocity vector of the particle, and T and T_p are the temperature of the gas phase at the particle position and the temperature of the particle, respectively.

The particle response and thermal response times are modeled as

$$\tau^u = \frac{\rho_p d_p^2}{18\mu f_u(Re_p)} \tag{11}$$

and

$$\tau^\theta = \frac{c_{p,p}\rho_p d_p^2}{12k f_\theta(Re_p)}, \tag{12}$$

where $c_{p,p}$ is the specific heat of the particle, d_p is the diameter of the particle, ρ_p is the density of the particle, and μ is the dynamic viscosity of the gas phase evaluated at the particle position. Since Re_p is typically larger than unity, we use the following correlation[21] for Stokes' drag

$$f_u(Re_p) = 1 + 0.15 Re_p^{0.687} \tag{13}$$

and the Ranz-Marshall correlation[22] for energy

$$f_\theta(Re_p) = 1 + 0.3 Re_p^{1/2} Pr^{1/3}, \tag{14}$$

where the particle Reynold number is

$$Re_p = \frac{d_p|\boldsymbol{V} - \boldsymbol{V}_p|}{\nu}. \tag{15}$$

Here, ν is the kinematic viscosity of gas at the particle position. Forces exerted by particles on the fluid are

$$\boldsymbol{f}_p = -\sum \frac{\pi d_p^3 \rho_p}{6\tau^u}(\boldsymbol{V_p} - \boldsymbol{V}), \tag{16}$$

where $\sum$ denotes summation over all the particles within the finite volume cell. Energy transfer from each individual particle to the surrounding fluid is governed by

$$E_p = \sum \left[\boldsymbol{f}_p \cdot (\boldsymbol{V}_p - \boldsymbol{V}) - \frac{\pi d_p^3 \rho_p c_{p,p}}{6\tau^\theta}(T_p - T) \right]. \tag{17}$$

Ffowcs-Williams Hawkings Solver

Lighthill[23] derived the acoustic analogy by rearranging the Navier-Stokes equations into an inhomogeneous wave equation with an equivalent source term. Ffowcs-Williams and Hawkings[24] used generalized functions and included the effects of surfaces in arbitrary motion in the context of the wave equation. The FWH equation as originally proposed is

$$\left(\frac{1}{c^2}\frac{\partial^2}{\partial t^2} - \frac{\partial^2}{\partial x_i^2} \right) p' = \frac{\partial}{\partial t}\left[\rho_\infty \mathcal{U}_{n'}\right]\delta(g) - \frac{\partial}{\partial x_i}\left[p n_i' \delta(g)\right] + \frac{\partial^2}{\partial x_i \partial x_j}\left[\mathcal{T}_{ij}\mathcal{H}(g)\right], \tag{18}$$

and for a penetrable porous surface[25] is

$$\left(\frac{1}{c^2}\frac{\partial^2}{\partial t^2} - \frac{\partial^2}{\partial x_i^2} \right) p' = \frac{\partial}{\partial t}\left[\rho_\infty U_{n'}\right]\delta(g) - \frac{\partial}{\partial x_i}\left[L_i \delta(g)\right] + \frac{\partial^2}{\partial x_i \partial x_j}\left[\mathcal{T}_{ij}\mathcal{H}(g)\right], \tag{19}$$

where $U_{n'} = (1-\rho\rho_\infty^{-1})\mathcal{U}_{n'} + \rho\mathcal{V}_{n'}\rho_\infty^{-1}$, $L_i = p\delta_{ij}n_j' + \rho\mathcal{V}_i(\mathcal{V}_{n'} - \mathcal{U}_{n'})$, and $\mathcal{T}_{ij} = \rho\mathcal{V}_i\mathcal{V}_j - \sigma_{ij} + (p' - c_\infty^2\rho')\delta_{ij}$. Note that $\mathcal{T}_{ij}$ is the Lighthill stress tensor, σ_{ij} is the viscous stress tensor, $\mathcal{H}(g)$ is the Heaviside function, and $\delta(g)$ is the Dirac delta function. The first and second term on the right hand side of Eqn. 18 and 19 represents the acoustic monopole and dipole source terms on the porous surface, while the last term represents the acoustic quadrupole source in the volume surrounding the body.

The FWH surface is defined by an equation of the form $g(x,t) = 0$ subject to $\nabla \boldsymbol{g} = \boldsymbol{n'}$, where $\boldsymbol{g}$ is a space and time function representing the surface and $\boldsymbol{n'}$ is the unit outward normal to the surface. We assume p' is acoustic pressure when the fluctuations in density are very small compared to the ambient density (i.e. $\rho'\rho_\infty^{-1} << 1$). The acoustic pressure is $p' = c_\infty^2\rho' = c_\infty^2(\rho - \rho_\infty)$, where c_∞ is the ambient speed of sound. The variables p, $\boldsymbol{\mathcal{V}}$, and $\boldsymbol{\mathcal{U}}$ are the local static pressure, the flow velocity, and the velocity with which the surface moves, respectively.

Extension of Farassat's Formulation

Farassat[26] derived his Formulation 2B from Eqn. 18 to predict pressure in the far-field from the FWH surface when the flow velocity is zero. We position a FWH surface plane, which represent the porous surfaces, within the flow-field that encloses the turbulence of the jet plume. The velocity fluctuations are non-zero on the porous surface. We follow the formulation of Farassat[26] and derive additional source terms that contain velocity fluctuations. We find

$$\begin{aligned} 4\pi p'(x,t) = \int_{-\infty}^{\infty} \Bigg[& \frac{\rho_\infty \dot{\mathcal{U}}_{n'}}{r(1-M_r)^2} + \frac{\rho_\infty \mathcal{U}_{n'}(r\dot{M}_r + c(M_r - M^2))}{r^2(1-M_r)^3} + \frac{\dot{\ell}_r}{cr(1-M_r)^2} + \frac{\ell_r - \ell_i \cdot M_i}{r^2(1-M_r)^2} \\ & + \frac{\ell_r(r\dot{M}_r + c(M_r - M^2))}{cr^2(1-M_r)^3} + \left(\frac{\dot{\rho}(\mathcal{V}_{n'} - \mathcal{U}_{n'}) + \rho(\dot{\mathcal{V}}_{n'} - \dot{\mathcal{U}}_{n'})}{r(1-M_r)^2} \right)(1 + \mathcal{M}_r) + \frac{\rho(\mathcal{V}_{n'} - \mathcal{U}_{n'})}{r(1-M_r)^2}\dot{\mathcal{M}}_r \\ & + \frac{\rho(\mathcal{V}_{n'} - \mathcal{U}_{n'})(\mathcal{V}_r - \mathcal{V}_i M_i)}{r^2(1-M_r)^2} + \frac{\rho(\mathcal{V}_{n'} - \mathcal{U}_{n'})(1 + \mathcal{M}_r)}{r^2(1-M_r)^3}(r\dot{M}_r + c(M_r - M^2)) \Bigg]_{ret} dS, \end{aligned} \tag{20}$$

where, $r = |\boldsymbol{x} - \boldsymbol{y}|$ is the distance from each location of the porous surface $\boldsymbol{y}$ to the observer location $\boldsymbol{x}$, $\boldsymbol{M}$ and $\boldsymbol{\mathcal{M}}$ denotes the Mach number of the surface velocity and flow velocity, respectively with components $M_i = \mathcal{U}_i c_\infty^{-1}$ and $\mathcal{M}_i = \mathcal{V}_i c_\infty^{-1}$. The variable $\ell_i = p \cdot n_i'$ is the component of the local force intensity that acts on the fluid. A dot over the variable represents the time derivative. The subscript $\boldsymbol{r}$ denotes the dot product for any given quantity with the unit radiation vector. The subscript *ret* means that the quantities inside the bracket are evaluated at the retarded time. The area of each face on the FWH surface is denoted by dS.

We elect to keep the FWH surface stationary relative to the nozzle. Hence, we can substitute $\boldsymbol{\mathcal{U}} = 0$ and $\boldsymbol{M} = 0$ into Eqn. 20 and simplify

$$4\pi p'(x,t) = \int_{-\infty}^{\infty} \left[\frac{\dot{\ell}_r}{cr} + \frac{\ell_r}{r^2} + \left(\frac{\dot{\rho}\mathcal{V}_{n'} + \rho\dot{\mathcal{V}}_{n'}}{r} \right) (1 + \mathcal{M}_r) + \frac{\rho\mathcal{V}_{n'}}{r}\dot{\mathcal{M}}_r + \frac{\rho\mathcal{V}_{n'}\mathcal{V}_r}{r^2} \right]_{ret} dS. \tag{21}$$

Geometry and Computational Domain

We include the nozzle geometry within the computational domain to capture its effect on the resultant flow physics. Furthermore, the effect of the nozzle boundary layer is captured, including its effect on its interaction with the plate attached to the nozzle exit. The shock waves emerging from within the nozzle due to the divergent section are also captured in the prediction. The nozzle modeled is a two-dimensional representation of the rectangular nozzle used in the experimental study.[15] Figure 1 shows the geometry of the nozzle. The nozzle has a design Mach number, M_d, of 1.5. The walls within the convergent and divergent sections of the nozzle are planar. The height of the nozzle inlet, h_i, throat, h_t, and outlet, h_e, are 2.5908×10^{-2} m, 1.0973×10^{-2} m, and 1.2954×10^{-2} m, respectively. The nozzle used in experiment of Mora et al.[15] has a spanwise width, w_e, of 0.25908×10^{-2} m, hence the aspect ratio of the nozzle exit is two. The equivalent nozzle exit diameter, D_e ($D_e = 2(\pi^{-1}h_e w_e)^{1/2}$) is 2.065×10^{-2} m. The total length of the nozzle is 0.1 m. The computational domain extends $100h_e$ ($62.7D_e$) from the nozzle exit in the downstream direction. It extends $10h_e$ ($6.3D_e$) in the upstream direction from the nozzle exit and $20h_e$ ($12.5D_e$) in the cross-stream direction. A solid plate is attached at the bottom of the domain along $x = 0$, beginning from the exit of the nozzle and extending to the right end of the domain.

Figures 2 and 3 show the computational grid, which contains a total of 787,500 hexahedral cells. The minimum grid spacing is on the order of 10^{-5} m in both the streamwise and the cross-stream directions. We limit the largest grid point spacing to 200 times of the smallest. We created the computational grid using three sub-domains. The first is internal to the nozzle and contains a refined plume region. This region contains 2000 cells in the streamwise direction and 100 cells in the cross-stream direction. The second consists of a region around the shear layer and contains 1500 cells in the streamwise direction and 100 cells in the cross-stream direction. Finally, the third region resides within the domain outside the shear layer and upstream from the nozzle exit. This sub-domain has 1750 cells in the streamwise direction and 250 cells in the cross-stream direction. The cells are highly clustered to resolve the boundary layer along the plate, the shear layer that extends downstream from the nozzle lip (near the nozzle throat), and in the nozzle exit plane. This clustering is chosen to capture as many flow structures as possible.

Boundary Conditions

Three flow conditions from the experiment of Mora et al.[15] with fully expanded Mach numbers of M_j =1.22, 1.5, 1.64 are chosen for this study. The corresponding nozzle pressure ratio (NPR), which is the ratio of total pressure at the nozzle inlet to the ambient static pressure p_∞, are 2.5, 3.67, and 4.5, respectively. The nozzle inlet plane uses a stagnation inlet boundary condition, where the total pressure and total temperature are held constant. The inlet velocity and other thermodynamic quantities are allowed to vary. Different total pressure ratios corresponding to NPRs of 2.50, 3.67, and 4.50 are prescribed at the inlet of the nozzle for corresponding Mach numbers. The total temperature ratio (TTR) is held constant at 1.10, which is the ratio of stagnation temperature in the plenum divided by the ambient static temperature. In the multiphase cases particles are injected into the nozzle at nearly a constant rate, which mimics a solid rocket engine. We use an injection algorithm to ensure that the particle velocity is the same as the flow at the inlet of the nozzle. Also, the mass flux ratio of particles to gas at the inlet boundary condition is held constant. The mass flux ratio of particles to gas at the inlet is 0.001, and two cases with particle diameter, d_p, of 10 μm and 100 μm are studied. Super particle loading of 10 is used for particles of diameter, $d_p = 10$ μm, so that a super particle represents 10 real particles with same properties. The super particle loading for the $d_p = 100$ μm case is unity. The no-slip and adiabatic boundary conditions are enforced on the internal wall of the nozzle and the plate trailing the nozzle, while the external wall and lip of the nozzle are slip walls to enhance numerical stability. Particles reflect from the walls with no energy loss. When particles leave the computational domain, they are removed from the calculation. The upper, left, and right boundaries of the

domain are prescribed as far-field boundary condition with a free-stream Mach number of $M_\infty = 0.01$, in the streamwise direction for numerical stability, pressure $p_\infty = 101325$ Pa, and static temperature $T_\infty = 293$ K.

Implementation of the Retarded Time Algorithm for the FWH Equation

Formulation 2B (Eqn. 21) of Farassat is evaluated to predict the far-field acoustic pressure as a function of time and observer position. We evaluate Eqn. 21 using the retarded time algorithm described by Brentner.[27] All the quantities derived in Eqn. 21 are sampled with various FWH surfaces from CFD calculations and are used as input to the acoustic solver. The face areas, face centers, and face normals are derived based upon the cell connectivity of the porous surface. Using the retarded time algorithm, we march in time at the observer location, and calculate the retarded time by spherically spreading the sound signal back to the porous surface. We also assume that no refraction effects occur outside the FWH surface. If the porous surface is stationary relative to the statistically stationary turbulence, we assume that the retarded time is related to observer time as $\tau = t - rc_\infty^{-1}$. Note that t is not dependent on the location of the porous surface with respect to the observer. Acoustic radiation from a point on the porous surface far from the observer has a longer propagation time relative to a point which is closer to the observer. The retarded time obtained may not necessarily match with the time dependent CFD data, so interpolation is used to obtain the retarded time quantities. Interpolated quantities are substituted into Eqn. 21. Each face of the porous surface contributes to the total fluctuating acoustic pressure. These contributions are summed to find the resulting total acoustic radiation from the turbulent flow-field.

Results

Aerodynamics

Figures 4 and 5 show the time-averaged numerical schlieren of flow with M_j of 1.5 and 1.64. The shock-cell structure and its interaction with the shear layer and wall boundary layer are observed. The shock-cell structure is apparent downstream of the nozzle throat within both the on- and off-design jets. This is due to the bi-conic shape of the nozzle that features a sharp angle at the nozzle throat and a straight divergent section. In the $M_j = 1.64$ case, the shock waves are stronger and have a greater impact on free shear layer. The second shock cell interacting with the shear layer causes a much more rapid change of shear layer growth for the $M_j = 1.64$ jet. In both M_j of 1.5 and 1.64 jets, strong directional acoustic radiation is observed propagating at angles of approximate 20 and 30 degrees, respectively, relative to the downstream nozzle axis. Numerical schlieren of the $M_j = 1.22$ jet is not included as it shows flow separation occurring within the nozzle, which is not consistent with the measurement. Recall that these simulations are two-dimensional, also our computational grid is too coarse to fully resolve the turbulent boundary layer. These limitations are present due to computational expense and are not due to the developed methodology. This may potentially cause the flow to separate.

Figures 6, 7, and 8 show time-averaged streamwise velocity on the centerline. Our predictions do not capture as many shocks as observed in measurement. Furthermore, our predicted mean streamwise velocity decays at a higher rate starting in the region of $x/D_e \approx 8$ to 12. Note that the current simulation is in two-dimensions, and the shock wave originating from the wall perpendicular to the spanwise direction is not represented. The turbulent structures within two-dimensional flows have longer time scales and spatial coherence than corresponding three-dimensional flows. Therefore, it is expected that the potential core is shorter in two-dimensional flows, which leads to a faster decay of streamwise velocity on the centerline.

The mean streamwise velocity and the normalized mean streamwise velocity are shown in Figures 9 and 10, respectively. These velocities are plotted for the fully expanded condition at the centerline of the nozzle for three different cases, i.e. single phase flow, flow with particles of diameter 10 μm, and flow with particles of diameter 100 μm. The mean velocity changes are within 15 m/s when comparing the 10 μm case with the single phase case, as seen in Figure 9. The mean velocity at the nozzle exit decreases drastically in the 100 μm case compared to the single phase case. Figure 10 shows that the length of the potential core is significantly longer because of the interaction of large particles with the flow. This shows large solid particles, even at very low mass fraction, withdraw energy from the flow constantly and suppress the growth of the shear layer. Equations 11 and 16 show that the drag force, $\boldsymbol{f}_p$, is proportional to the diameter of particles, d_p. The strong coupling of particles and gas phase also impacts the location of the expansion wave within the nozzle. The second expansion wave shifting downstream is shown in Figure 11 of mean pressure

on the centerline of the nozzle.

Figure 12 shows a contour plot of TKE for the case with particle sizes of 10 μm. We predict that the TKE is generated within the shear layer and close to the plate attached to the nozzle, where a large velocity gradient exists. The TKE greatly increases after the potential core ends ($\sim 10D_e$). Figure 13 shows the comparison of TKE on the lip line. The flow with particle diameters of 100 μm contains the least intense turbulence generation at the lip line of the three cases examined. The magnitude of TKE is comparable between the single phase case and the case with particles of 10 μm diameter. However, the turbulent eddies develop closer to the nozzle exit and becomes stronger for the case with particulates. As a consequence, the first peak of TKE shifts left in the two cases when the particulates are present.

Figures 14 and 15 show the instantaneous numerical schlieren of flow field with particle diameters of 10 and 100 μm, respectively. Blue points in the figures represent the location of aluminum particles. The distribution of particles in these two cases is significantly different. In the case where the particle diameters are 10 μm, particles mainly concentrate in the core region of the plume and subsequently form a saddle shape downstream of $5D_e$, due to the influence of large turbulent coherent structures. In the case of particle diameters of 100 μm, the particles spread into a cone shape that is larger than the plume. The saddle shape observed in Figure 14 is not observed in Figure 15, due to the higher inertia associated with particles of diameter 100 μm.

Aeroacoustics

Validation of the Ffowcs-Williams Hawkings Solver

We validate the FWH solver before acoustic predictions are conducted for the single and multiphase jets. Validation of the FWH solver and its implementation is conducted by comparing predictions with an analytical solution of a random superposition of monopoles, dipoles, and quadrupoles. Sources are placed at random positions within a sphere of radius 0.01 m. A spherical porous FWH surface is maintained at a 0.1 m radius. An observer is placed at 1 m from the origin of the porous sphere. The frequency and phase of each source is randomized. The analytical result is found through superposition of each source's corresponding solution at both the porous surface and at the observer. The FWH solver uses the analytical solution at the porous surface to predict the acoustic pressure at the test observer. Figure 16 shows a comparison of the FWH prediction with the analytical solution, where the y-axis is pressure and the x-axis is time. The L2-norm of the relative error between the predicted solution and the analytical solution is 0.0106, which is an acceptable error.

Validation of Aeroacoustic Predictions with Measurements

Predicted narrow-band sound spectra at a distance of $R = 40D_e$ and radiation angles from $\theta = 70°$ to $\theta = 152°$ of the $M_j = 1.64$ jet are shown in Figure 17. Here, θ is the radiation angle measured from the upstream nozzle centerline axis. Predictions suggest that Mach wave and large-scale turbulent mixing are the dominant source of noise, which is consistent with experiments. At $\theta = 70°$, predicted noise spectrum is compared with measured data as shown in Figure 18. Predicted spectra has an acceptable agreement with measurements below St number ($St = fD_e u_j^{-1}$) of unity, while larger inconsistency occur at higher frequency and an unphysical peak occurs at approximately St of 2. This is partly due to our choice of implicit LES and the limited number of grid points present within our simulations. Therefore, we are not capable of fully resolving fine-scale turbulent mixing noise and broadband shock-associated noise.

Figure 19 illustrates narrow-band SPL per unit St of the $M_j = 1.5$ jet at radiation angle $\theta = 152°$. Recall that our CFD simulation is performed in two-dimensions, and the FWH solver is applied over a finite range in the spanwise direction. This is not consistent with the experiment. Therefore, we calibrate the spanwise integration range for the FWH solver such that the overall sound pressure level matches the measurement in amplitude. The single noise peak at St number of approximately 0.2 is predicted accurately. The overall spectral shape also agrees with measurement data. The method captures the large-scale structures of turbulence and predicts the overall correct spectral shape.

Comparison of Single-Phase and Multi-Phase Predictions

Figures 20 and 21 show the cross-correlation of the component, $\mathcal{T}_{11}$, of the Lighthill stress tensor[23] at two points located D_e and $2D_e$ downstream of the nozzle exit on the lip line. The jet is slightly heated, and so

the effects of sound generation from non-linearity and viscosity are negligible compared to the other terms.[23] Hence, we approximate the Lighthill stress tensor, $\mathcal{T}_{ij}$, with $\rho V_i V_j$. Figure 20 illustrates that the sound source at these two points on the lip line are loosely correlated in all cases with or without particles. The strong periodicity observed in the cross-correlation curves shows that the large structures are convecting downstream and growing. It is shown in an enlarged view of the two-point cross-correlation, in Figure 21, that the convection time is approximately 70, 105, and 90 μs for the case without particle, with particles $d_p = 10\mu m$, and $d_p = 100\mu m$, respectively. Figures 22, 23 and 24 reveal more detail of the convection velocity of the sound source by showing the two-point cross-correlation at different streamwise separation distances, r, from the first point located D_e downstream on the lip line. The correlation curves are constructed with a cubic polynomial. The envelope curve, that connects the maximum correlation of different curves, is interpolated using a quadratic polynomial. Figure 22 is for the single phase case. The envelope shows a general linear decreasing trend till 40 μs then flattens out. It indicates that the convection velocity of ρuu remains constant and then slowly decreases in the case of pure gas. Figure 23 corresponds to the jet flow with particulates of $d_p = 10$ μm. The characteristics of $\mathcal{T}_{11}$ are very different relative to the single phase case. The convection velocity decreases very rapidly from $r/D_e = 0$ to 0.4 and changes very little after the separation distance is greater than $0.5D_e$. Figure 24 corresponds to the jet flow with particulates of $d_p = 100$ μm. The envelope is similar to that in Figure 23 until $r/D = 0.4$, then the envelope almost linearly decreases instead of flattening out in the case of particles with $d_p = 10$ μm. It reveals that the decay of convection velocity derived from ρuu is almost at a constant rate which is equal to the initial rate of the case with smaller particles.

Figures 25 and 26 show acoustic spectra of particle laden jets relative to the ideally expanded jet. The addition of particles of $d_p = 100$ μm suppresses the sound intensity at higher frequencies at all radiation angles, while the lower frequency noise is moderately increased. This is observed at the radiation angle of $\theta = 152°$, where the overall sound pressure level is largest due to the very intense noise radiated from turbulent eddies in the shear layer. The acoustic spectra of the flow with small particles are generally the same relative to single phase flow. It is also consistent with aerodynamic results presented in the previous section. However, the peak sound level shifts toward high frequency at the downstream observer location, especially at $\theta = 130°$ and $153°$.

Summary and Conclusion

In this paper, we establish a jet noise prediction method for fluid-particle two-phase flow that utilizes a two-stage implicit LES and FWH method. The CFD simulation uses an Eulerian-Lagrangian framework. Two-way coupling occurs through momentum and heat exchanges between the fluid and particles. The predictions are compared with the experiment of Mora et al.[15] We simulate real gas wall jets that operate at ideal, under-, and over-expanded conditions, with particles of diameter 10 μm and 100 μm. Noise predictions are conducted in the far-field and the acoustics spectra of single phase cases of $M_j = 1.5$ and 1.64 are validated with measurements and have acceptable agreement, given the simulation is performed in two-dimension. The impact of particles of different size are studied at the on-design condition. We observe that the smaller particles do not alter the flow field dramatically, while the larger particles greatly reduce the mean velocity and turbulent kinetic energy. The overall sound spectra changes with the addition of particles with varying diameter. Large particles increase low frequency noise while decreasing high frequency noise. The overall sound pressure level change is not significant when comparing the single phase case with the 10 μm case. However, the peak amplitude of the acoustic spectra shift toward higher frequencies.

We are pursuing three-dimensional CFD simulations of multiphase jets corresponding to solid fuel rocket engines. Through these simulations, we hope to capture the three-dimensional nature of turbulence for the purpose of characterizing changes in turbulent statistics and radiated noise due to multiphase effects.

Acknowledgments

We are especially grateful for valuable discussions with Dr. Thomas Jackson of the University of Florida Center for Compressible Multiphase Turbulence. This research is supported by the University of Florida Department of Mechanical and Aerospace Engineering and the Herbert Wertheim College of Engineering.

References

[1]Melcher, J. C., Krier, H., and Burton, R. L., "Burning Aluminum Particles Inside a Laboratory-Scale Solid Rocket Motor," *Journal of Propulsion and Power*, Vol. 18, No. 3, 2002, pp. 631–640. doi:10.2514/6.2001-3947.

[2]Dupays, J., "Two-Phase Unsteady Flow in Solid Rocket Motors," *Aerospace Science and Technology*, Vol. 6, No. 6, 2002, pp. 413 – 422. doi:10.1016/S1270-9638(02)01182-3.

[3]Beiting, E. J., "Solid Rocket Motor Exhaust Model for Alumina Particles in the Stratosphere," *Journal of spacecraft and rockets*, Vol. 34, No. 3, 1997, pp. 303–310. doi:10.2514/2.3233.

[4]Hermsen, R., "Aluminum Oxide Particle Size for Solid Rocket Motor Performance Prediction," *J. Spacecraft*, Vol. 18, No. 6, 1981, pp. 483–490. doi:10.2514/3.57845.

[5]Tam, C. K. W. and Auriault, L., "Jet Mixing Noise from Fine-Scale Turbulence," *AIAA Journal*, Vol. 37, No. 2, 1999, pp. 145–153. doi:10.2514/3.14141.

[6]Smith, M. J. and Miller, S. A. E., "The Effects of Surfaces on the Aerodynamics and Acoustics of Jet Flows," *19th AIAA/CEAS Aeroacoustics Conference*, AIAA Paper 2013-2041, 2013. doi:10.2514/6.2013-2041.

[7]Bremner, P., Blelloch, P., Hutchings, A., Shah, P., Streett, C., and Larsen, C., "Validation of Methods to Predict Vibration of a Panel in the Near Field of a Hot Supersonic Rocket Plume," *17th AIAA/CEAS Aeroacoustics Conference (32nd AIAA Aeroacoustics Conference)*, American Institute of Aeronautics and Astronautics, Jun 2011. doi:10.2514/6.2011-2852.

[8]Shur, M. L., Spalart, P. R., and Strelets, M. K., "Noise Prediction for Underexpanded Jets in Static and Flight Conditions," *AIAA Journal*, Vol. 49, No. 9, Sep 2011, pp. 2000–2017. doi:10.2514/1.j050776.

[9]Baier, F., Mora, P. A., Gutmark, E. J., and Kailasanath, K., "Flow Measurements from a Supersonic Rectangular Nozzle Exhausting Over a Flat Surface," *55th AIAA Aerospace Sciences Meeting*, AIAA Paper 2017-0932, Jan 2017. doi:10.2514/6.2017-0932.

[10]Balachandar, S. and Eaton, J. K., "Turbulent Dispersed Multiphase Flow," *Annual Review of Fluid Mechanics*, Vol. 42, No. 1, 2010, pp. 111–133. doi:10.1146/annurev.fluid.010908.165243.

[11]Gore, R. and Crowe, C., "Effect of Particle Size on Modulating Turbulent Intensity," *International Journal of Multiphase Flow*, Vol. 15, No. 2, 1989, pp. 279 – 285. doi:https://doi.org/10.1016/0301-9322(89)90076-1.

[12]Campos, L. M. B. C., Bourgine, A., and Bonomi, B., "Comparison of Theory and Experiment on Aeroacoustic Loads and Deflections," *Journal of Fluids and Structures*, Vol. 13, No. 1, 1999, pp. 3–35. doi:10.1006/jfls.1998.0192.

[13]Fukuda, K., Tsutsumi, S., Fujii, K., Ui, K., Ishii, T., Oinuma, H., Kazawa, J., and Minesugi, K., "Acoustic Measurement and Prediction of Solid Rockets in Static Firing Tests," *15th AIAA/CEAS Aeroacoustics Conference (30th AIAA Aeroacoustics Conference)*, AIAA Paper 2009-3368, May 2009. doi:10.2514/6.2009-3368.

[14]Heeb, N., Mora, P., Gutmark, E., and Kailasanath, K., "Investigation of the Noise from a Rectangular Supersonic Jet," *19th AIAA/CEAS Aeroacoustics Conference*, 2013, p. 2239. doi:10.2514/6.2013-2239.

[15]Mora, P., Baier, F., Kailasanath, K., and Gutmark, E. J., "Acoustics from a Rectangular Supersonic Nozzle Exhausting over a Flat Surface," *The Journal of the Acoustical Society of America*, Vol. 140, No. 6, dec 2016, pp. 4130–4141. doi:10.1121/1.4967158.

[16]Haselbacher, A., "RocfluMP Developer and Reference Manual," *Center for Simulation of Advanced Rockets, University of Illinois at Urbana-Champaign*, 2005.

[17]Najjar, F., Ferry, J., Haselbacher, A., and Balachandar, S., "Simulations of Solid-Propellant Rockets: Effects of Aluminum Droplet Size Distribution," *Journal of Spacecraft and Rockets*, Vol. 43, No. 6, 2006, pp. 1258–1270. doi:10.2514/1.17326.

[18]Annamalai, S., Rollin, B., Ouellet, F., Neal, C., Jackson, T. L., and Balachandar, S., "Effects of Initial Perturbations in the Early Moments of an Explosive Dispersal of Particles," *Journal of Fluids Engineering*, Vol. 138, No. 7, 2016, pp. 070903. doi:10.1115/1.4030954.

[19]Haselbacher, A. C., Balachandar, S., and Kieffer, S., "Open-Ended Shock Tube Flows: Influence of Pressure Ratio and Diaphragm Position," *AIAA journal*, Vol. 45, No. 8, 2007, pp. 1917–1929. doi:10.2514/1.23081.

[20]Miller, S. A. E., "Theoretical Aeroacoustics: Compiled Mathematical Derivations of Fereidoun 'Feri' Farassat," NASA/TM-2016-219179, 2016.

[21]Naumann, Z. and Schiller, L., "A Drag Coefficient Correlation," *Z. Ver Deutsch. Ing*, Vol. 77, 1935, pp. 318–323.

[22]Ranz, W., Marshall, W. R., et al., "Evaporation from Drops," *Chemical Engineering Progress*, Vol. 48, No. 3, 1952, pp. 141–146.

[23]Lighthill, M. J., "On Sound Generated Aerodynamically. I. General Theory," *Proceedings of the Royal Society A: Mathematical, Physical and Engineering Sciences*, Vol. 211, No. 1107, Mar 1952, pp. 564–587. doi:10.1098/rspa.1952.0060.

[24]Ffowcs-Williams, J. E. and Hawkings, D. L., "Sound Generation by Turbulence and Surfaces in Arbitrary Motion," *Philosophical Transactions of the Royal Society of London A: Mathematical, Physical and Engineering Sciences*, Vol. 264, No. 1151, 1969, pp. 321–342. doi:10.1098/rsta.1969.0031.

[25]Farassat, F. and Casper, J., "Broadband Noise Prediction when Turbulence Simulation is Available – Derivation of Formulation 2B and its Statistical Analysis," *Journal of Sound and Vibration*, Vol. 331, No. 10, 2012, pp. 2203–2208. doi:10.1016/j.jsv.2011.07.044.

[26]Farassat, F., "Derivation of Formulations 1 and 1A of Farassat," NASA/TM-2007-214853, 2007.

[27]Brentner, K. S. and Farassat, F., "Modeling Aerodynamically Generated Sound of Helicopter Rotors," *Progress in Aerospace Sciences*, Vol. 39, No. 2, 2003, pp. 83 – 120. doi:10.1016/S0376-0421(02)00068-4.

Figures

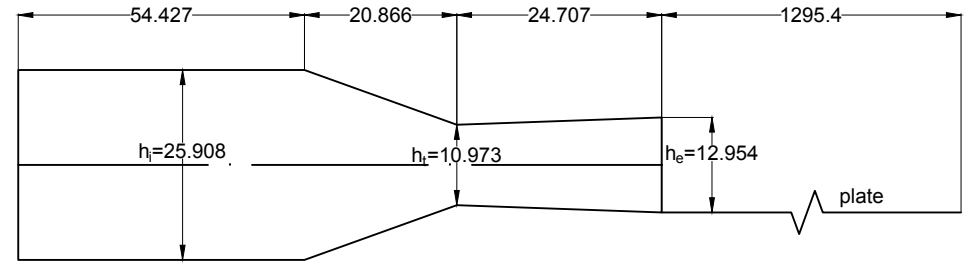

Figure 1. Side view of the nozzle geometry with units in mm.

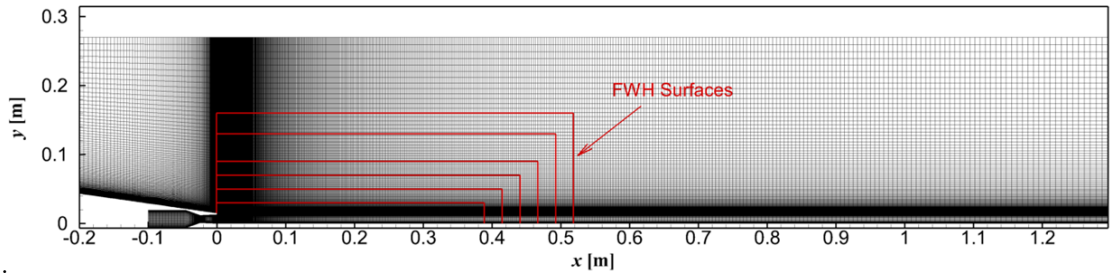

Figure 2. The computational grid and location of the FWH surfaces.

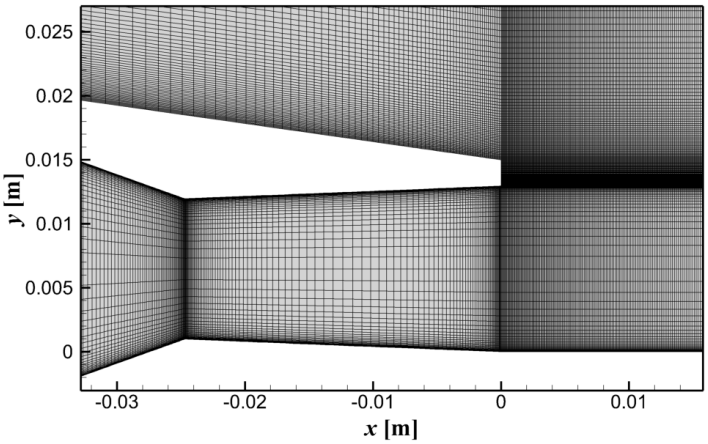

Figure 3. Details of the computational grid near the nozzle exit.

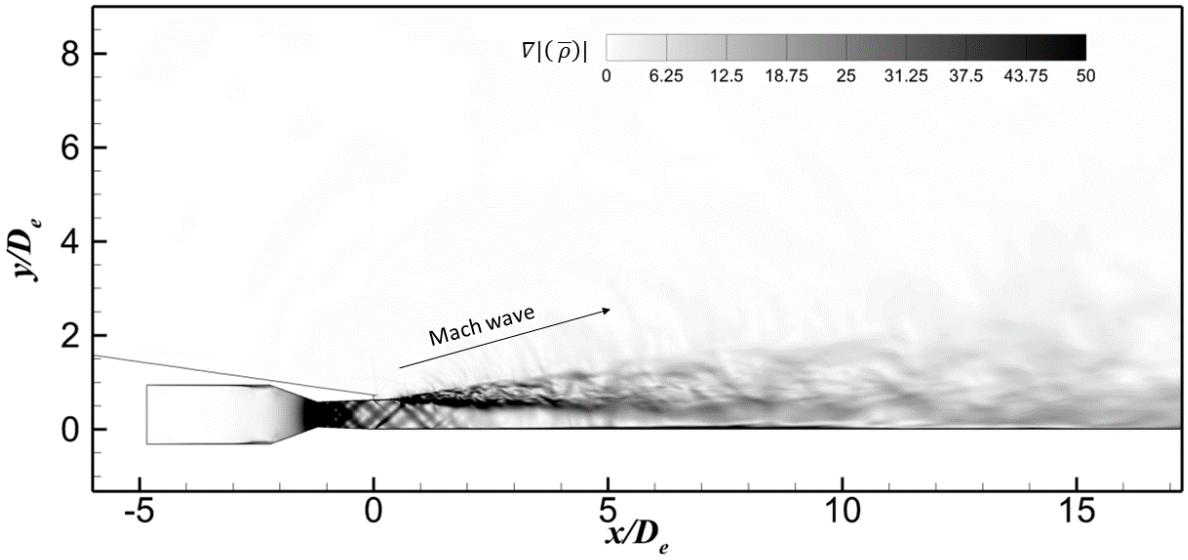

Figure 4. Time-average of the magnitude of the density gradient (numerical schlieren) for $M_j = 1.5$.

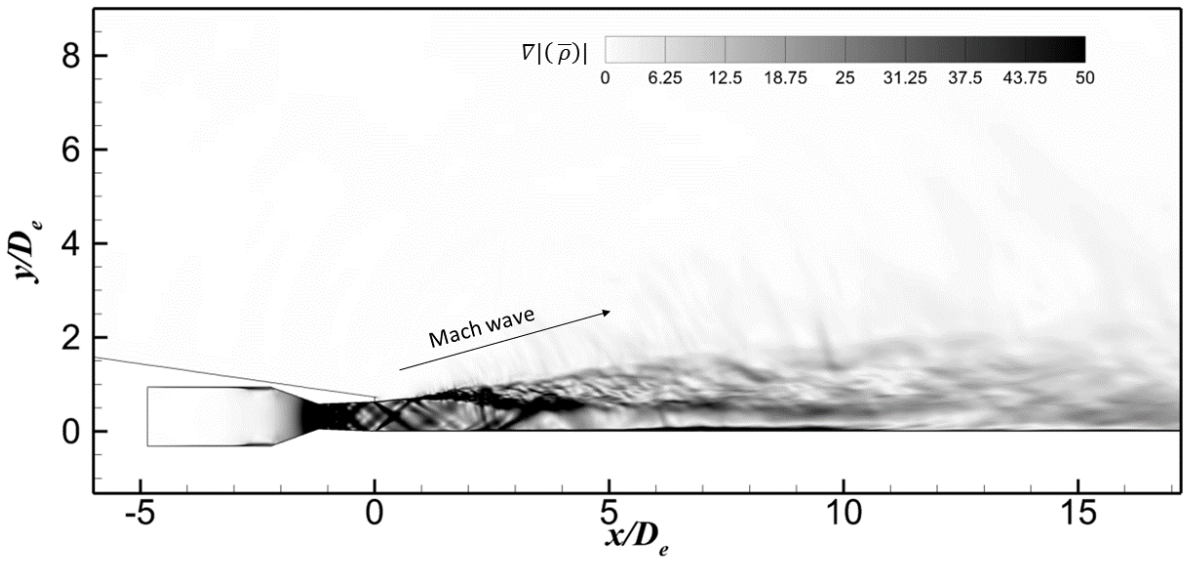

Figure 5. Time-average of the magnitude of the density gradient (numerical schlieren) for $M_j = 1.64$.

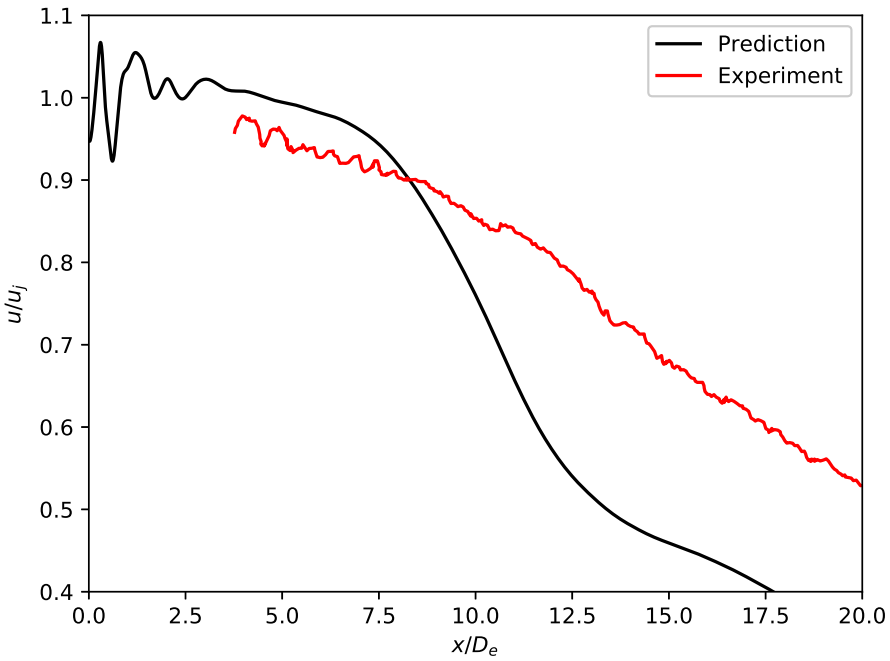

Figure 6. Comparison of predicted and measured (see Baier et al.[9]) time averaged streamwise velocity on the centerline for $M_j = 1.22$.

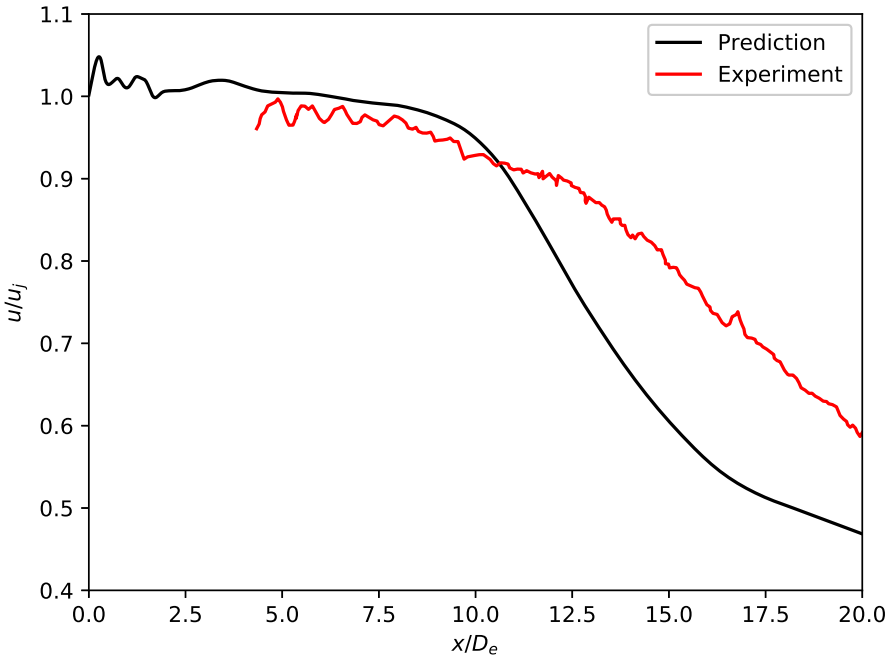

Figure 7. Comparison of predicted and measured (see Baier et al.[9]) time averaged streamwise velocity on the centerline for $M_j = 1.5$.

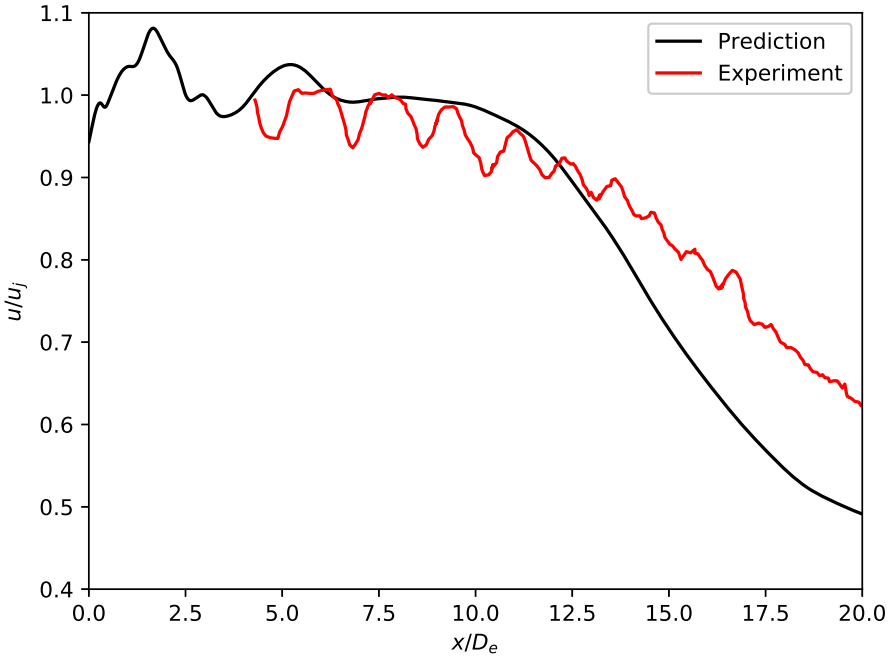

Figure 8. Comparison of predicted and measured (see Baier et al.[9]) time averaged streamwise velocity on the centerline for $M_j = 1.64$.

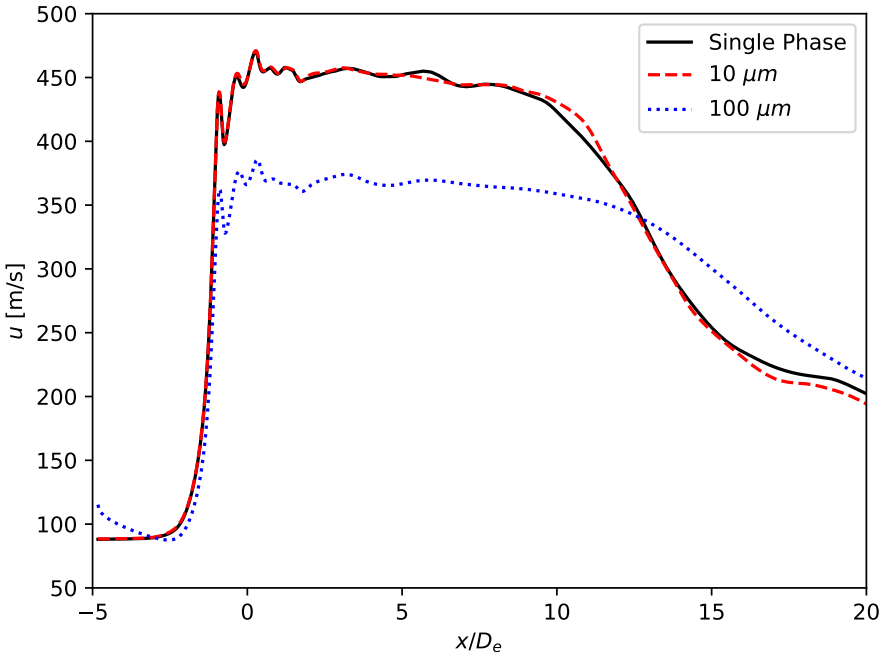

Figure 9. Mean velocity on the centerline of the nozzle.

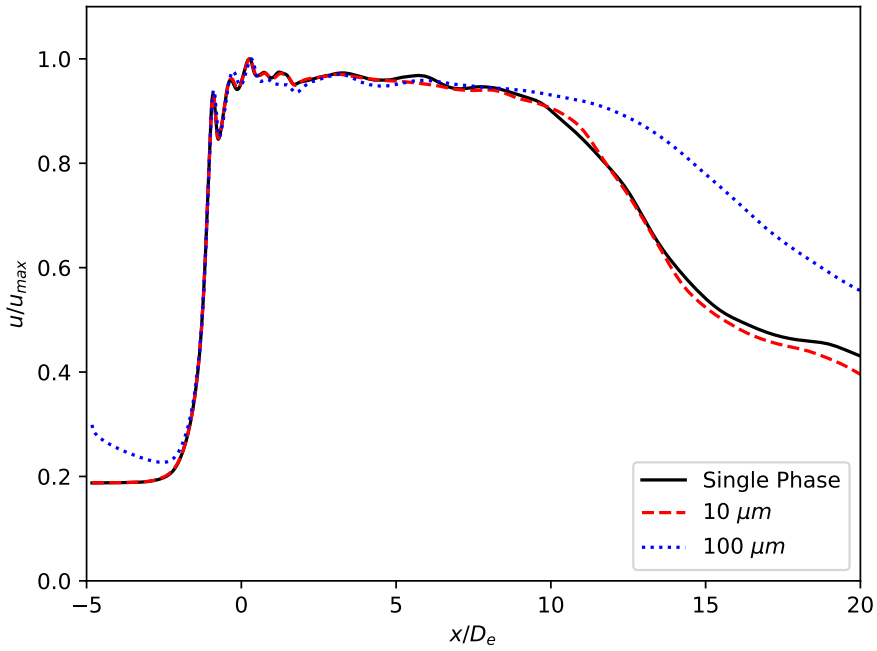

Figure 10. Normalized mean velocity on the centerline of the nozzle.

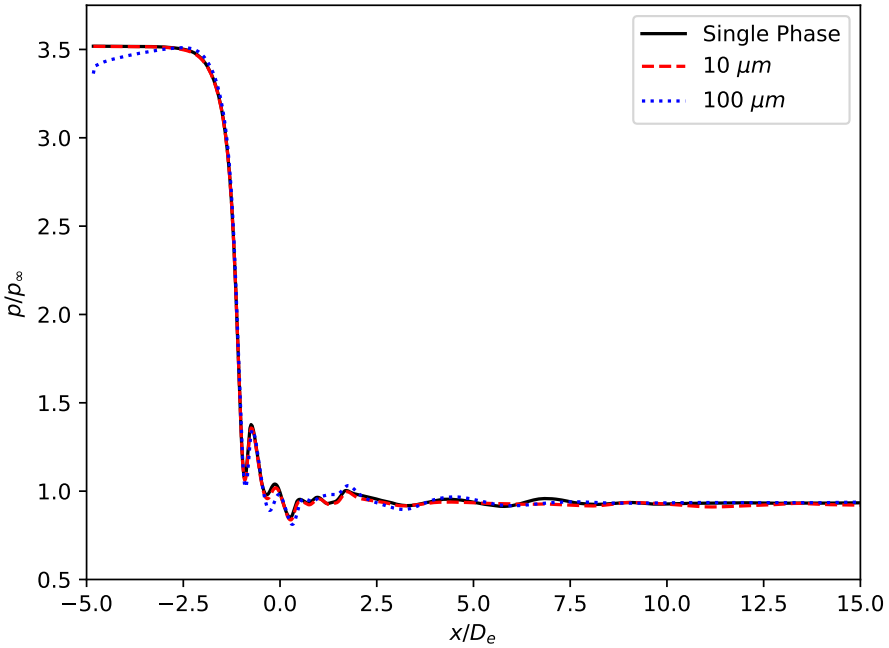

Figure 11. Mean pressure on the centerline of the nozzle.

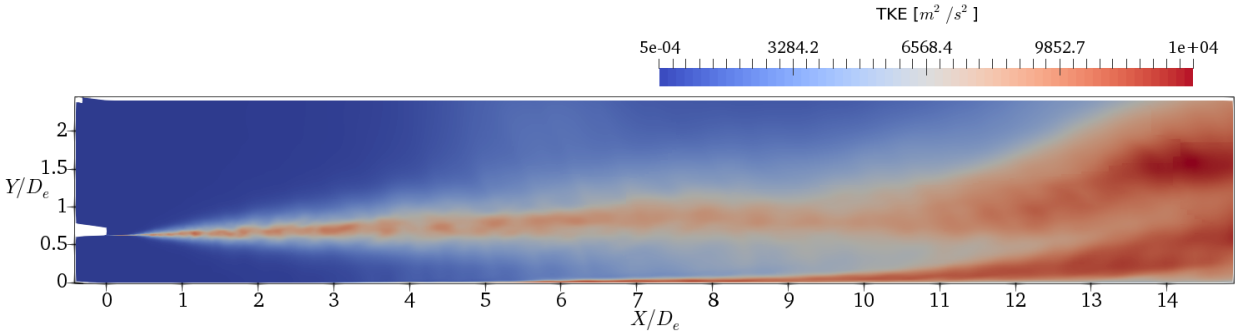

Figure 12. Contour of TKE.

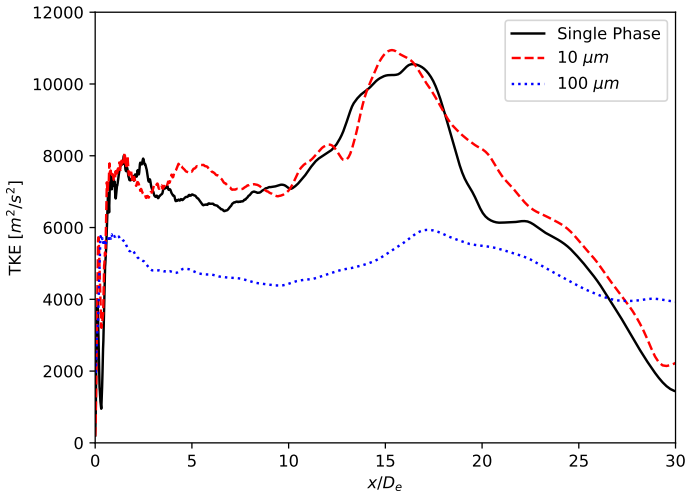

Figure 13. Turbulent kinetic energy, k, on the lip line with various particle sizes.

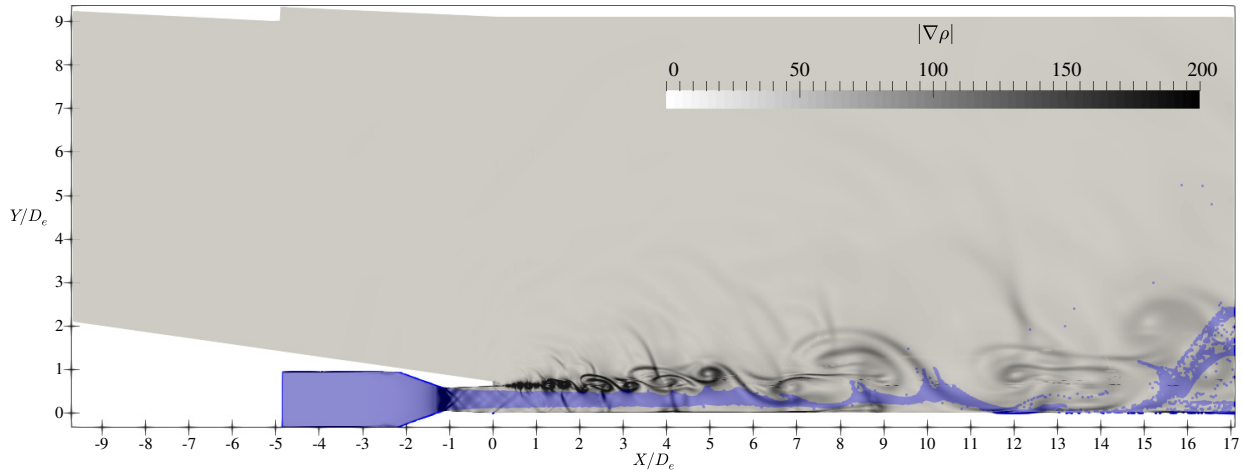

Figure 14. Instantaneous magnitude of density gradient (numerical schlieren) for the case with particle diameter of 10 μm. The blue dots represent particle locations.

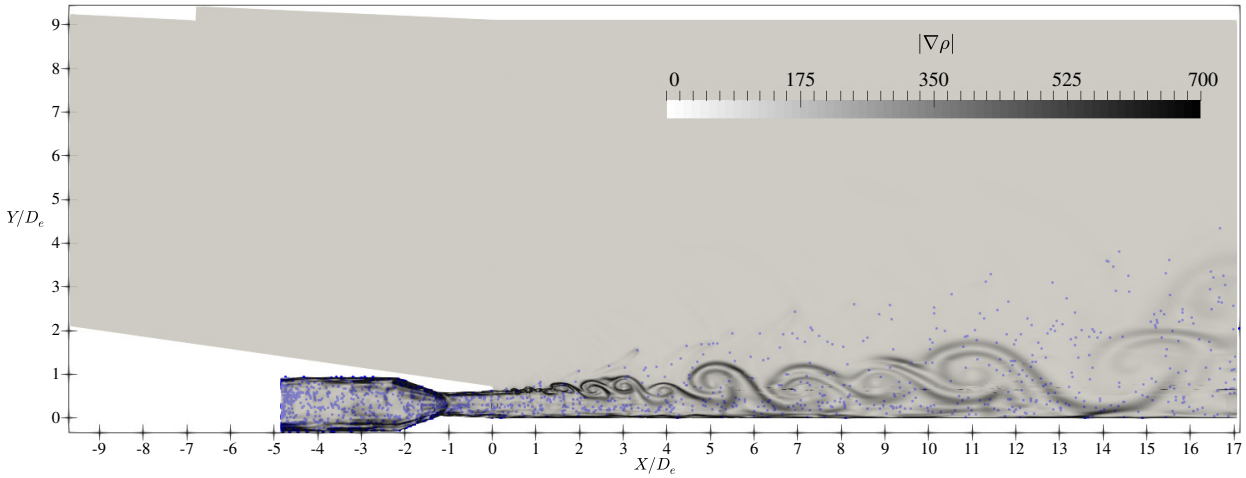

Figure 15. Instantaneous magnitude of density gradient (numerical schlieren) for the case with particle diameter of 100 μm. The blue dots represent particle locations.

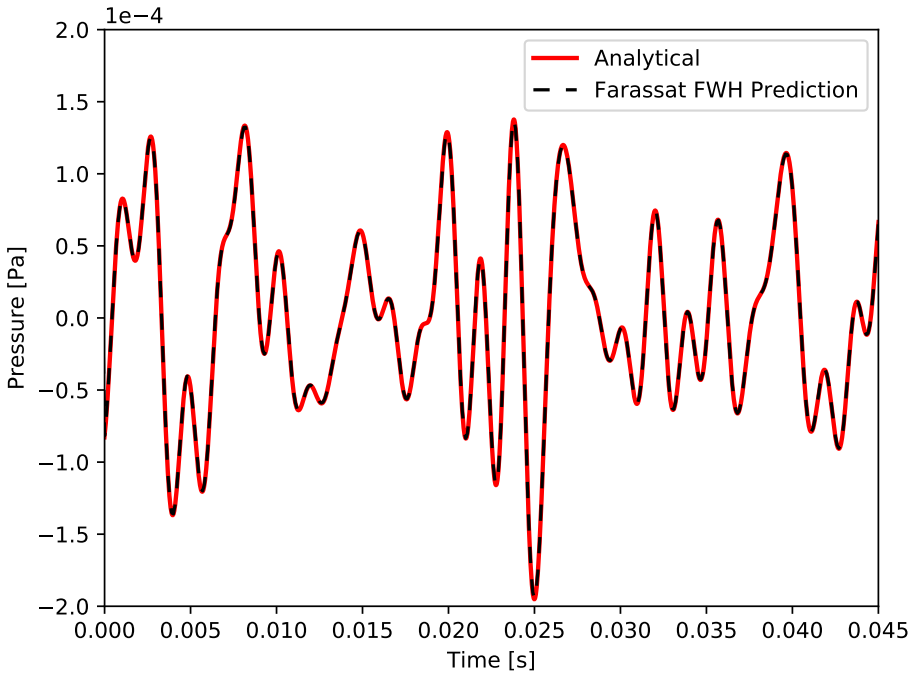

Figure 16. Comparison of Farassat's formulation for multiple monopoles, dipoles and quadruples with analytical solution.

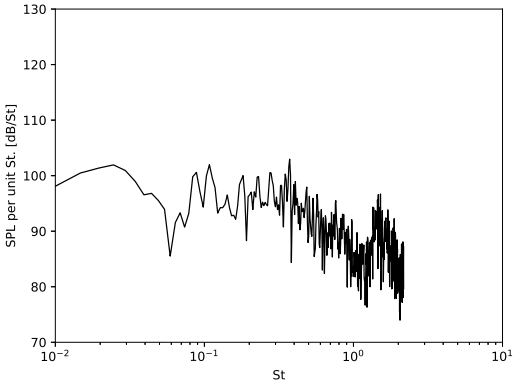

(a) $\theta = 70°$

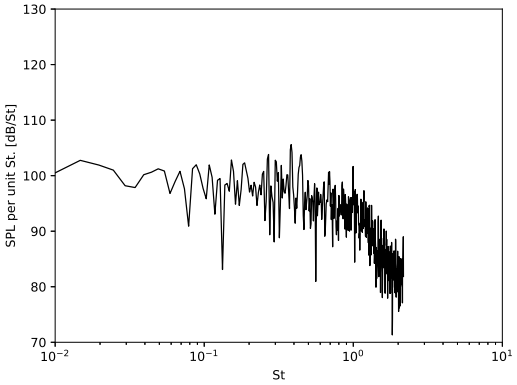

(b) $\theta = 90°$

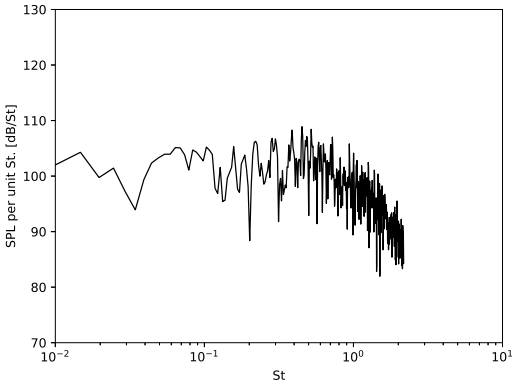

(c) $\theta = 110°$

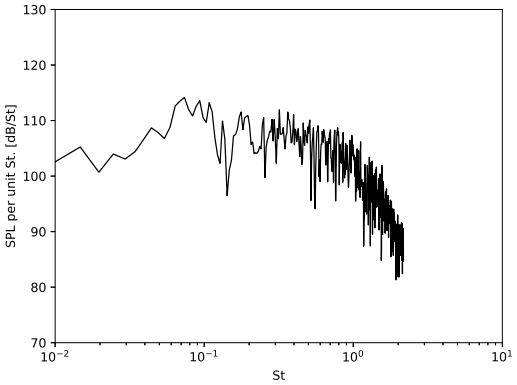

(d) $\theta = 130°$

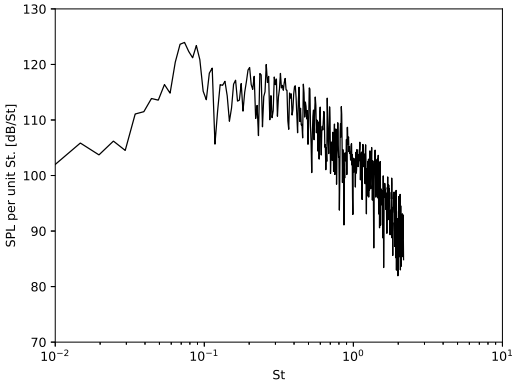

(e) $\theta = 152°$

Figure 17. Far-field noise SPL spectra for the $M_j = 1.64$ jet. Microphones are located $40D_e$ away from the intersection of the nozzle exit plane and centerline.

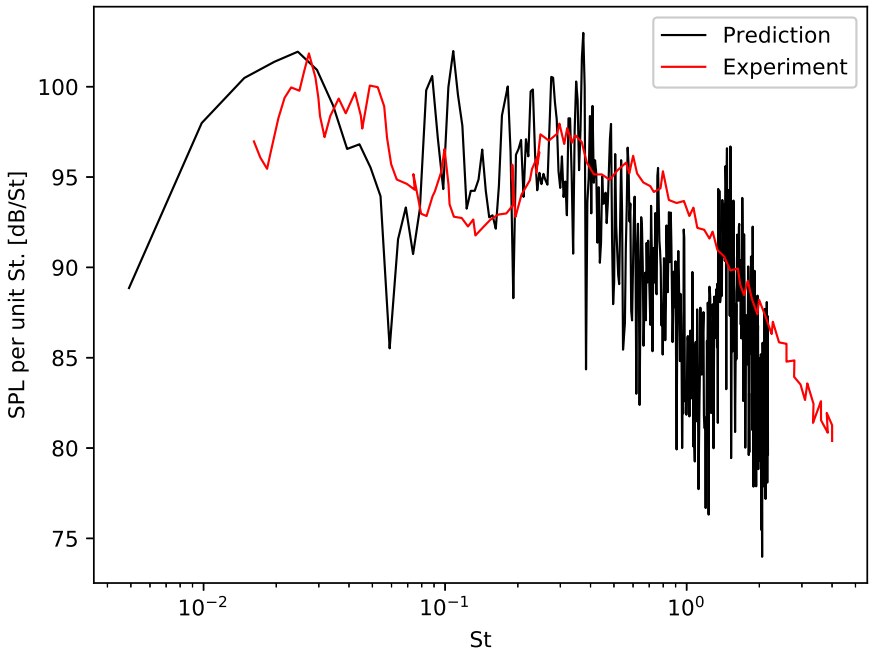

Figure 18. Comparison of predicted and measured (see Mora et al.[15]) SPL spectra for $M_j = 1.64$ at $\theta = 70^\circ$ and $R = 40D_e$.

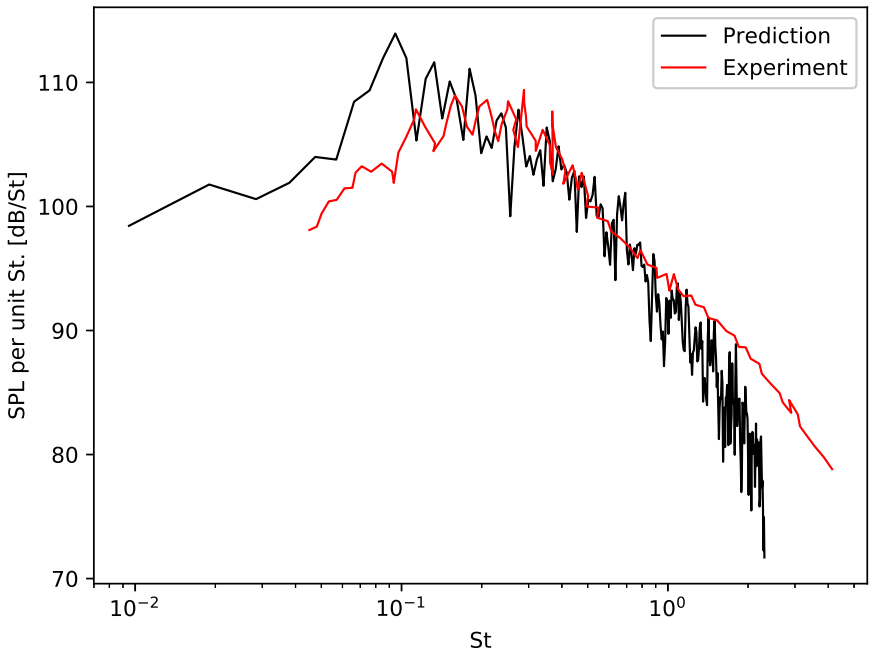

Figure 19. Comparison of predicted and measured (see Mora et al.[15]) SPL spectra for $M_j = 1.5$ at $\theta = 152^\circ$ and $R = 40D_e$.

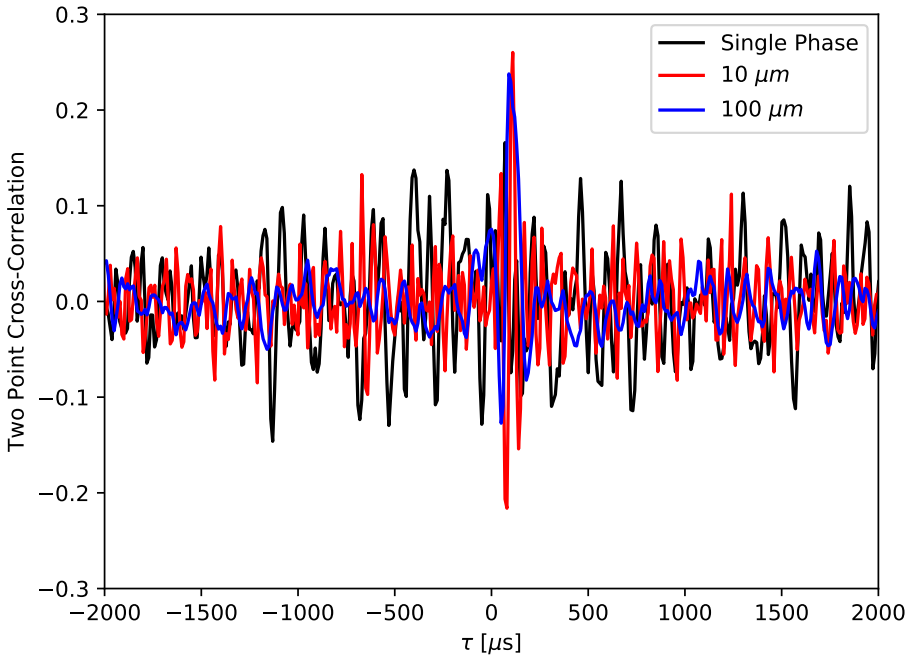

Figure 20. Two-point cross-correlation of $\mathcal{T}_{11}$ of Lighthill's stress tensor. Sampling points are at $X_1 = D_e$, $Y_1 = D_e$, $X_2 = 2D_e$, and $Y_2 = D_e$.

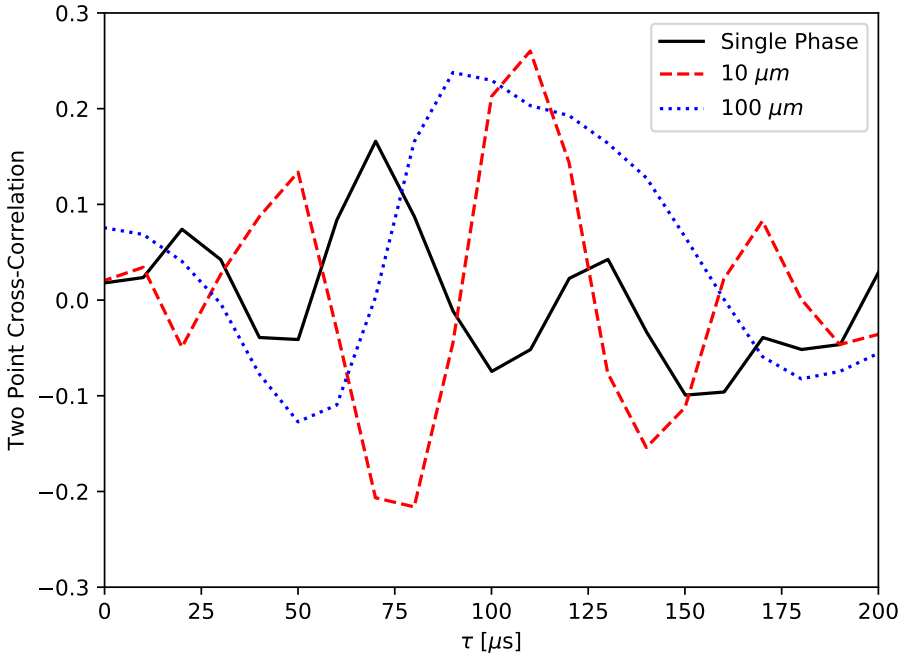

Figure 21. Two-point cross-correlation of $\mathcal{T}_{11}$ of Lighthill's stress tensor (limited range near the peaks). Sampling points are at $X_1 = D_e$, $Y_1 = D_e$, $X_2 = 2D_e$, and $Y_2 = D_e$.

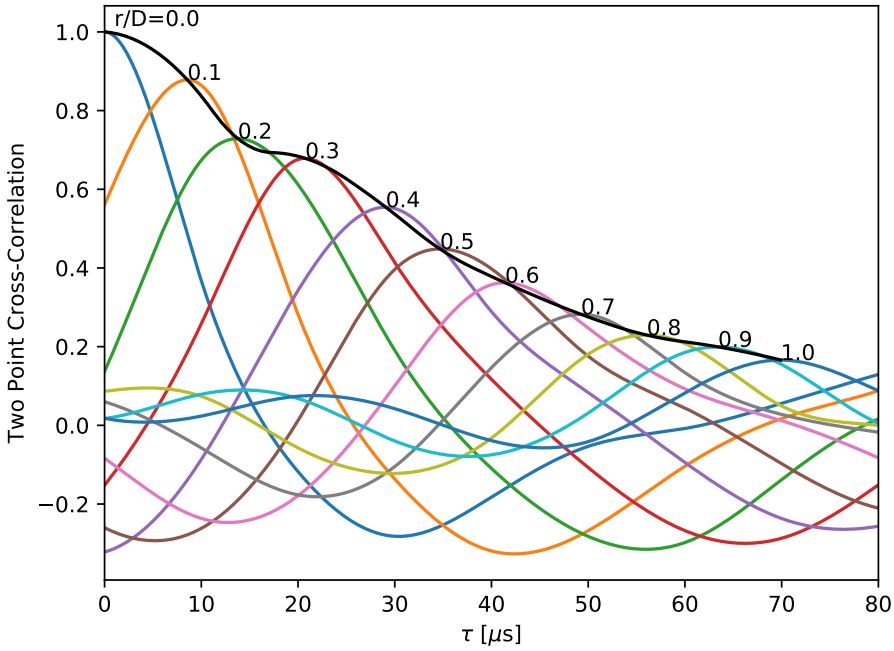

Figure 22. Cross-correlation of Lighthill's stress tensor ($\mathcal{T}_{11}$) without any particulates with streamwise separation, r, at $X = D_e$ and $Y = D_e$.

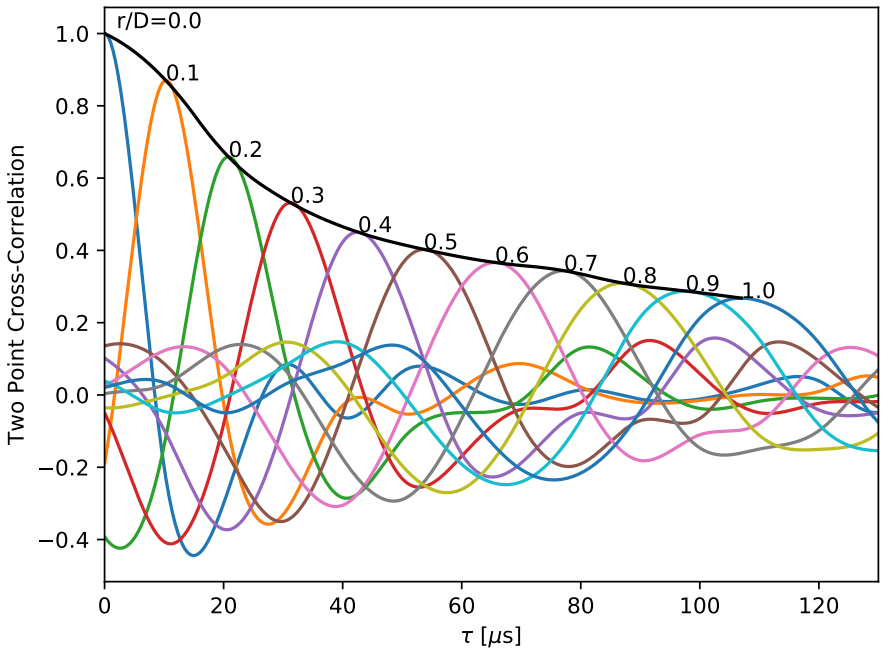

Figure 23. Cross-correlation of Lighthill's stress tensor ($\mathcal{T}_{11}$) for the 10 μm case with streamwise separation, r, at $X = D_e$ and $Y = D_e$.

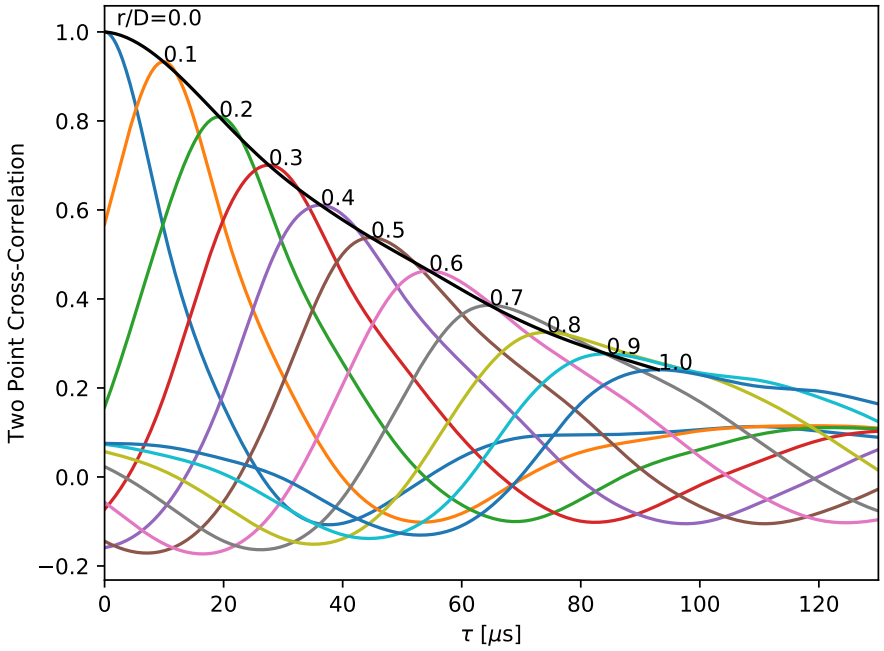

Figure 24. Cross-correlation of Lighthill's stress tensor ($\mathcal{T}_{11}$) for the 100 μm case with streamwise separation, r, at $X = D_e$ and $Y = D_e$.

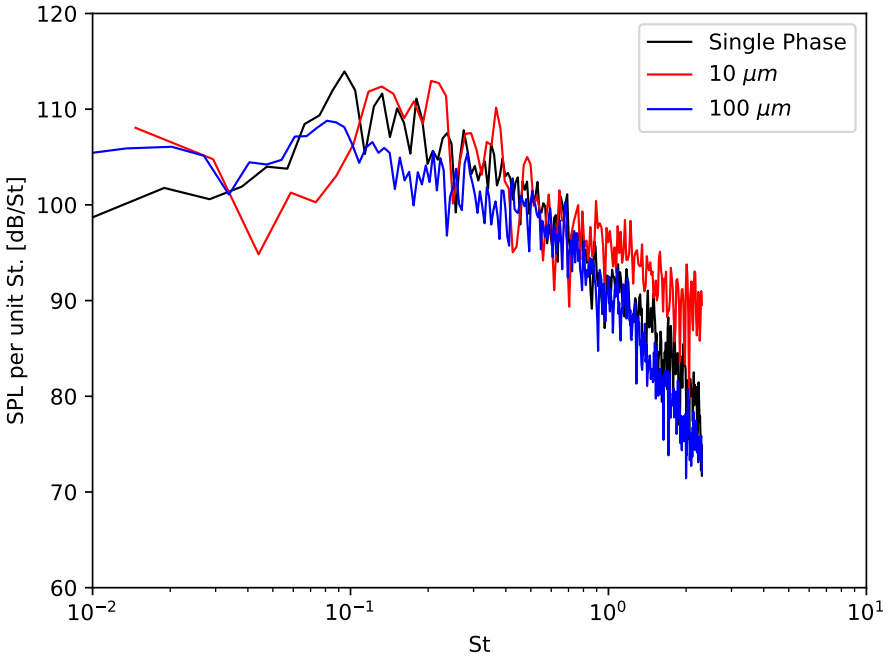

Figure 25. Comparison of SPL spectra for various particle sizes for $M_j = 1.5$ at $\theta = 152^\circ$ and $R = 40D_e$.

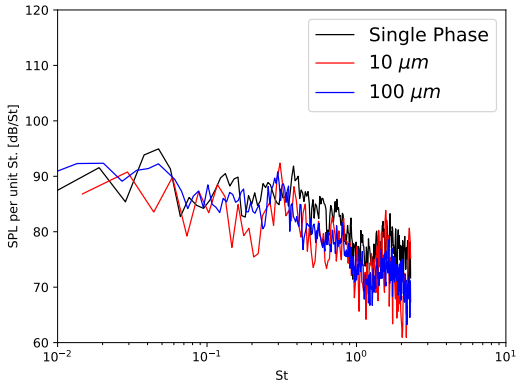

(a) $\theta = 70°$

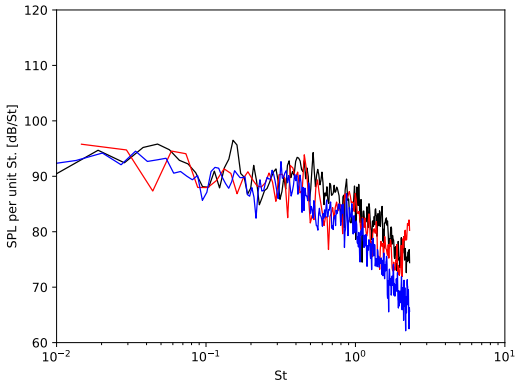

(b) $\theta = 90°$

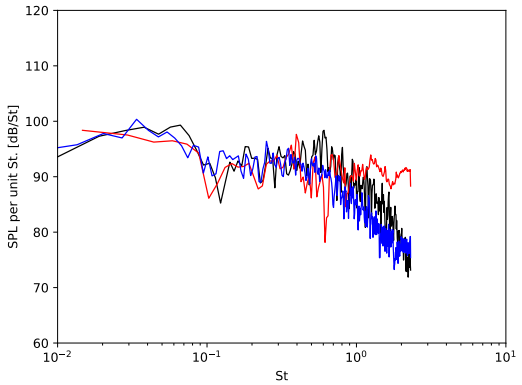

(c) $\theta = 110°$

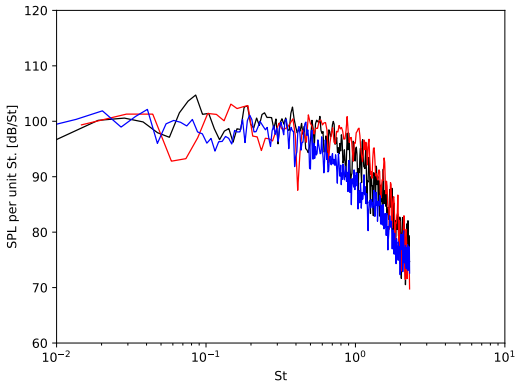

(d) $\theta = 130°$

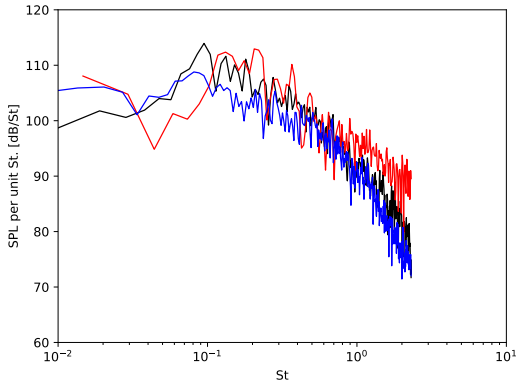

(e) $\theta = 152°$

Figure 26. Far-field noise SPL spectra for the $M_j = 1.5$ jet without particles and with particles of diameter, d_p, of 10 and 100 μm. Microphones are located $40D_e$ away from the intersection of nozzle exit plane and centerline.